



In-situ Switchback Formation in the Expanding Solar Wind

J. Squire¹, B. D. G. Chandran², and R. Meyrand¹¹ Physics Department, University of Otago, Dunedin 9010, New Zealand; jonathan.squire@otago.ac.nz² Department of Physics and Astronomy, University of New Hampshire, Durham, NH 03824, USA

Received 2020 January 23; revised 2020 February 6; accepted 2020 February 11; published 2020 February 26

Abstract

Recent near-Sun solar-wind observations from *Parker Solar Probe* have found a highly dynamic magnetic environment, permeated by abrupt radial-field reversals, or “switchbacks.” We show that many features of the observed turbulence are reproduced by a spectrum of Alfvénic fluctuations advected by a radially expanding flow. Starting from simple superpositions of low-amplitude outward-propagating waves, our expanding-box compressible magnetohydrodynamic simulations naturally develop switchbacks because (i) the normalized amplitude of waves grows due to expansion and (ii) fluctuations evolve toward spherical polarization (i.e., nearly constant field strength). These results suggest that switchbacks form in situ in the expanding solar wind and are not indicative of impulsive processes in the chromosphere or corona.

Unified Astronomy Thesaurus concepts: [Space plasmas \(1544\)](#); [Alfvén waves \(23\)](#); [Solar wind \(1534\)](#); [Solar magnetic fields \(1503\)](#); [Interplanetary turbulence \(830\)](#)

1. Introduction

The recent perihelion passes of *Parker Solar Probe* (*PSP*) have revealed a highly dynamic near-Sun solar wind (Bale et al. 2019; Kasper et al. 2019). A particularly extreme feature compared to solar-wind plasma at greater distances is the abundance of “switchbacks”: sudden reversals of the radial magnetic field associated with sharp increases in the radial plasma flow (Neugebauer & Goldstein 2013; Horbury et al. 2018, 2020). Such structures generally maintain a nearly constant field strength $|\mathbf{B}|$, despite large changes to \mathbf{B} . It remains unclear how switchbacks originate and whether they are caused by sudden or impulsive events in the chromosphere or corona (e.g., Roberts et al. 2018; Tenerani et al. 2020).

In this Letter, our goal is to illustrate that turbulence with strong similarities to that observed by *PSP* develops from simple, random initial conditions within the magnetohydrodynamic (MHD) model. Using numerical simulations, we show that constant- $|\mathbf{B}|$ radial-field reversals arise naturally when Alfvénic fluctuations grow to amplitudes that are comparable to the mean field. We hypothesize that the effect is driven by magnetic-pressure forces, which, by forcing $|\mathbf{B}|$ to be nearly constant across the domain (Cohen & Kulsrud 1974; Vasquez & Hollweg 1998), cause large- $\delta B_{\perp}/B_0$ fluctuations to become discontinuous (Roberts 2012; Valentini et al. 2019). The effect is most pronounced around $\beta \sim 1$ (where β is the ratio of thermal to magnetic pressure). Due to the radial expansion of the solar wind, initially small-amplitude waves propagating outward from the chromosphere naturally evolve into such conditions (van Ballegoijen et al. 2011; Perez & Chandran 2013; Montagud-Camps et al. 2018). We solve the MHD “expanding-box” equations (Grappin et al. 1993), which approximate a small patch of wind moving outward in the inner heliosphere. We deliberately keep the simulations simple, initializing with random superpositions of outward-propagating waves, assuming a constant wind velocity, and using an isothermal equation of state. That this generic setup reproduces many features of the turbulence and field statistics seen by *PSP* strongly suggests that switchbacks form in situ in the solar wind and are not remnants of impulsive or bursty events at the Sun.

2. Methods

We solve the isothermal MHD equations in the “expanding-box” frame (Grappin et al. 1993), which moves outward in the radial (x) direction at the mean solar-wind velocity, while expanding in the perpendicular (y and z) directions due to the spherical geometry. We impose a mean anti-radial (sunward) field $\mathbf{B}_0 = -B_{x0}\hat{x}$, with initial Alfvén speed $v_A = B_{x0}/\sqrt{4\pi\rho}$. The mass density ρ , flow velocity \mathbf{u} , and magnetic field \mathbf{B} evolve according to

$$\partial_t \rho + \tilde{\nabla} \cdot (\rho \mathbf{u}) = -2 \frac{\dot{a}}{a} \rho, \quad (1)$$

$$\partial_t \mathbf{u} + \mathbf{u} \cdot \tilde{\nabla} \mathbf{u} = -\frac{1}{\rho} \tilde{\nabla} \left[c_s^2(t) \rho + \frac{B^2}{8\pi} \right] + \frac{\mathbf{B} \cdot \tilde{\nabla} \mathbf{B}}{4\pi\rho} - \frac{\dot{a}}{a} \mathbb{T} \cdot \mathbf{u}, \quad (2)$$

$$\partial_t \mathbf{B} + \mathbf{u} \cdot \tilde{\nabla} \mathbf{B} = \mathbf{B} \cdot \tilde{\nabla} \mathbf{u} - \mathbf{B} \tilde{\nabla} \cdot \mathbf{u} - \frac{\dot{a}}{a} \mathbb{L} \cdot \mathbf{B}. \quad (3)$$

Here $\mathbb{T} = (0, 1, 1)$ and $\mathbb{L} = (2, 1, 1)$, $a(t) = 1 + \dot{a}t$ is the current perpendicular expansion with \dot{a}/a the expansion rate, and $\tilde{\nabla} \equiv (\partial_x, a^{-1}\partial_y, a^{-1}\partial_z)$ is the gradient operator in the frame comoving with the expanding flow. The equation of state is isothermal, but with a sound speed $c_s(t)$ that changes in time to mimic the cooling that occurs as the plasma expands (for adiabatic expansion, $c_s^2 \propto a(t)^{-4/3}$). A detailed derivation of Equations (1)–(3) is given in, e.g., Grappin et al. (1993) and Dong et al. (2014). The anisotropic expansion causes plasma motions and magnetic fields to decay in time. Those that vary slowly compared to \dot{a}/a scale as $B_x/\sqrt{\rho} \propto a^{-1}$, $B_{\perp}/\sqrt{\rho} \propto a^0$, $u_x \propto a^0$, $u_{\perp} \propto a^{-1}$, with $\rho \propto a^{-2}$ (Grappin & Velli 1996). In contrast, for small-amplitude Alfvén waves with frequencies $\gg \dot{a}/a$, $B_{\perp}/B_x \propto a^{1/2}$, and $u_{\perp}/v_A \propto a^{1/2}$. By appropriate parameter choices, we ensure that it is primarily this latter WKB effect that leads to large $\delta B_{\perp}/B_0$ waves in our simulations. The former non-WKB effect preferentially grows

$B_{\perp}/\sqrt{\rho}$ compared to u_{\perp} , thus acting like a reflection term for largest-scale waves and aiding in the generation of turbulence.

2.1. General Considerations

In order to simulate the propagation of Alfvénic fluctuations from the transition region to *PSP*'s first perihelion, our simulations would ideally have the following two properties:

- (i) Large expansion factor. As a parcel of solar-wind plasma flows from $r_i \simeq 1R_{\odot}$ to $r_f \simeq 35R_{\odot}$, it expands by a factor exceeding 35 because of super-radial expansion in the corona, leading (at least in the absence of dissipation) to a large increase in normalized fluctuation amplitudes.
- (ii) Minimum dissipation. The damping of inertial-range Alfvénic fluctuations is negligible, aside from nonlinear damping processes (turbulence, parametric decay, etc.).

Unfortunately, these properties are difficult to achieve: property (i) causes the numerical grid to become highly anisotropic, which can cause numerical instabilities, while property (ii) requires large numerical grids and careful choice of dissipation properties. Further, probing smaller scales deeper in the inertial range (as commonly done with elongated boxes in turbulence studies; Maron & Goldreich 2001) necessitates a slower expansion rate, which makes (ii) even more difficult to achieve because of the long simulation times. Our parameter scan and numerical methods are designed to investigate the basic physics of solar-wind turbulence within these limitations.

2.2. Numerical Methods

For the reasons discussed above, we use two separate numerical methods to solve Equations (1)–(3), which have different strengths and provide complementary results. The first—a modified version of the pseudospectral code Snoopy (Lesur & Longaretti 2007)—allows for larger expansion factors, making it possible to probe the growth of turbulence and switchbacks from low-amplitude waves. The second—a modified version of the finite-volume code Athena++ (Stone et al. 2008; White et al. 2016)—is better suited for capturing shocks and sharp discontinuities, but develops numerical instabilities for $a \gtrsim 4$. In Snoopy, we solve Equations (1)–(3) using $\ln \rho$ and $\mathbf{p} \equiv \rho \mathbf{u}$ as variables, applying the $\tilde{\nabla}$ operator by making the k_y and k_z grids shrink in time. We use sixth-order hyper-dissipation to regularize \mathbf{p} , \mathbf{B} , and $\ln \rho$, with separate time-varying parallel and perpendicular diffusion coefficients chosen to ensure that the Reynolds number remains approximately constant as the box expands. In Athena++, we use variables $\mathbf{B}'_{\perp} = \mathbf{B}_{\perp}/a$ and $\mathbf{u}'_{\perp} = \mathbf{u}_{\perp}/a$, which leads to MHD-like equations with a modified magnetic pressure (Shi et al. 2020). We use a simple modification of the HLLD Reimann solver of Mignone (2007) with second-order spatial reconstruction, without explicit resistivity or viscosity.

2.3. Simulation Parameters and Initial Conditions

Our simulations are listed in Table 1. Each starts with randomly phased, “outward-propagating” (z^+) Alfvén waves with $\mathbf{u}_{\perp} = \mathbf{B}_{\perp}$ and $u_x = 0$. The initial normalized fluctuation amplitude $\langle B_{\perp 0}^2 \rangle / B_{x0}^2 = \langle B_{y0}^2 + B_{z0}^2 \rangle / B_{x0}^2$ in each simulation varies between 0.2 and 1. To explore the range of power spectra that might be present in the low corona (see, e.g., van Ballegooijen et al. 2011; Chandran & Perez 2019), we consider three types of initial magnetic power spectra $E_{\perp 0}(k)$ in our

simulations: (i) isotropic spectra peaked at large scales, including Gaussian spectra $[E_{\perp 0}(k) \propto \exp(-k^2/k_0^2)]$ with $k_0 = 12/L_{\perp}$ and $E_{\perp 0}(k) \propto k^{-3}$; (ii) isotropic spectra with equal power across all scales $[E_{\perp 0}(k) \propto k^{-1}]$; and (iii) critically balanced spectra $E_{\perp 0}(k_{\perp}, k_{\parallel}) \propto k_{\perp}^{-10/3} \exp(-k_{\parallel} L_{\perp}^{1/3} / k_{\perp}^{2/3})$, which we denote with the shorthand “ $k_{\perp}^{-5/3}, k_{\parallel}^{-2}$ ” in Table 1, corresponding to the one-dimensional perpendicular and parallel spectra in the critical-balance model (Goldreich & Sridhar 1995; Cho et al. 2002). We avoid imposing any specific features on the flow or field (e.g., large-scale streams; Shi et al. 2020). Two additional simulation parameters are $c_s^2(t)$, which determines β through $\beta = 8\pi c_s^2(t) \langle \rho / B^2 \rangle$, and the expansion rate

$$\Gamma_{\text{sim}} \equiv \frac{\dot{a} L_x}{a v_A}, \quad (4)$$

which is the ratio of outer-scale Alfvén time L_x/v_A to expansion time $(\dot{a}/a)^{-1}$. In our simulations, Γ_{sim} is constant because $v_A \propto a^{-1}$, while \dot{a} and L_x are constant.³

Since most of the fluctuations propagate away from the Sun at speed v_A in the plasma frame, we map position x in the simulation to time t in the perihelion (zero-radial-velocity) *PSP* frame by setting

$$t = \frac{x}{U + v_A} + \text{constant}. \quad (5)$$

We then convert from simulation units to physical units by equating \dot{a}/a in the simulations with U/r . We set $r = 35R_{\odot}$, $U = 300 \text{ km s}^{-1}$, and $v_A = 115 \text{ km s}^{-1}$, values that approximate the conditions during *PSP*'s first perihelion pass (Bale et al. 2019; Kasper et al. 2019). The parallel box length L_x then corresponds via Equation (4) to the physical length scale $4.8 \times 10^6 \Gamma_{\text{sim}} \text{ km}$. An outward-propagating Alfvén wave with parallel wavelength L_x has a frequency

$$\frac{U + v_A}{L_x} = 8.7 \times 10^{-5} \left(\frac{\Gamma_{\text{sim}}}{0.5} \right)^{-1} \text{ Hz} \quad (6)$$

in the spacecraft frame. The smallest resolvable parallel wavelength, approximately four times the grid scale, corresponds to an Alfvén-wave frequency $(N_{\parallel}/4) \times (U + v_A)/L_x$, where N_{\parallel} is the number of grid points in the x direction.

The Snoopy simulations, labeled SW-#, are designed to optimize property (i) of Section 2.1. They start from small-amplitude waves, $\langle B_{\perp 0}^2 \rangle / B_{x0}^2 = 0.2$, and expand by a factor of $a_f/a_i = 10$ to reach large normalized amplitudes. We prescribe non-adiabatic temperature evolution $c_s^2(t) = 0.35t^{-1}$ for these runs, causing β to increase from $\beta \approx 0.2$ to $\beta \approx 1$ (Figure 1(a)), in approximate agreement with near-Sun predictions from the model of Chandran et al. (2011) with parameters chosen to match conditions seen by *PSP* (see Chen et al. 2020). The amplitude increases broadly as expected, with some dissipation, as shown in Figure 1(b). In contrast, the Athena++ simulations (labeled $\beta\#\text{-}\#$) are designed to explore the basic physics of expanding-box turbulence at a range of β values. They are limited to $a_f/a_i \lesssim 4$ by numerical instabilities, which necessitates starting from larger wave amplitudes, $\langle B_{\perp 0}^2 \rangle / B_{x0}^2 = 1.0$. The fluctuations rapidly (within less than an Alfvén time) develop broadband turbulence and near-constant

³ By assuming constant \dot{a} , our simulations do not capture the variable expansion rate of the solar wind at small R (see Tenerani & Velli 2017).

Table 1
Properties of the Simulations Studied in This Work (β is Shown in Figure 1(a))

Name	Resolution	Code	$(\frac{L_x}{L_\perp^i}, \frac{L_\perp^f}{L_\perp^i})$	$\frac{\dot{a} L_x}{a v_A}$	$\frac{\langle B_{\perp 0}^2 \rangle}{B_{x0}^2}$	Spectrum
SW-GS	480 ³	Snoopy	(4, 10)	2	0.2	$k_\perp^{-5/3}, k_\parallel^{-2}$
SW-Gaus	480 ³	Snoopy	(4, 10)	2	0.2	Gaussian
SW-s1	480 ³	Snoopy	(4, 10)	2	0.2	k^{-1}
SW-GS-LR	240 ³	Snoopy	(4, 10)	2	0.2	$k_\perp^{-5/3}, k_\parallel^{-2}$
β 1-Gaus-HR	540 × 1120 ²	Athena++	(1, 4)	0.5	1.0	Gaussian
β 1-GS	280 × 540 ²	Athena++	(1, 4)	0.5	1.0	$k_\perp^{-5/3}, k_\parallel^{-2}$
β 1-Gaus	280 × 540 ²	Athena++	(1, 4)	0.5	1.0	Gaussian
β 1-s1	280 × 540 ²	Athena++	(1, 4)	0.5	1.0	k^{-1}
β 1-s3	280 × 540 ²	Athena++	(1, 4)	0.5	1.0	k^{-3}
β 0.1-GS	280 × 540 ²	Athena++	(1, 4)	0.5	1.0	$k_\perp^{-5/3}, k_\parallel^{-2}$
β 0.02-GS	280 × 540 ²	Athena++	(1, 3)	0.5	1.0	$k_\perp^{-5/3}, k_\parallel^{-2}$
β 35-GS	280 × 540 ²	Athena++	(1, 4)	0.5	1.0	$k_\perp^{-5/3}, k_\parallel^{-2}$
β 1- \dot{a} 0.2	280 × 540 ²	Athena++	(1, 4)	0.2	1.0	$k_\perp^{-5/3}, k_\parallel^{-2}$
β 1- \dot{a} 0	280 × 540 ²	Athena++	(1, 1)	0	1.0	$k_\perp^{-5/3}, k_\parallel^{-2}$

Note. L_\perp^i and L_\perp^f are the initial and final perpendicular box size.

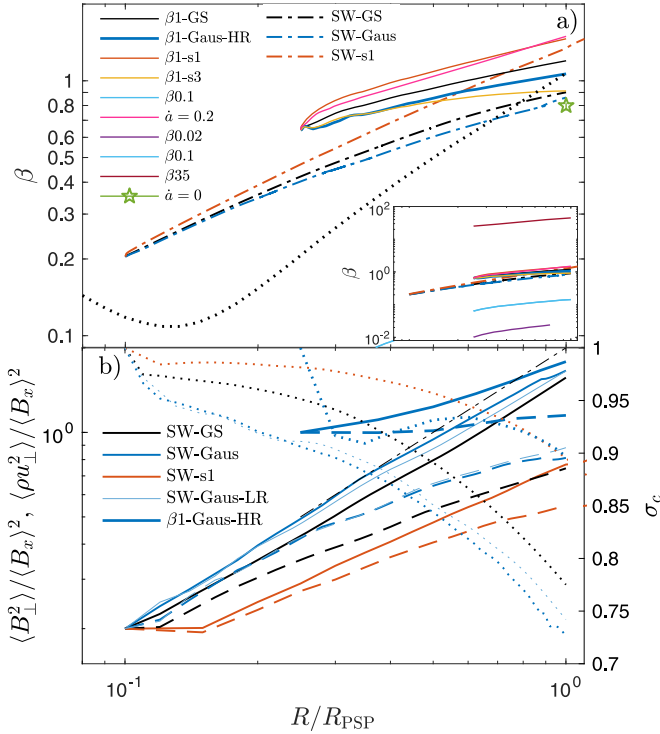


Figure 1. Radial evolution of simulation plasma properties. Panel (a) shows β for each simulation as labeled. The Snoopy simulations (dotted–dashed lines) crudely approximate β evolution from the model of Chandran et al. (2011) adapted to match the slow wind seen during *PSP*’s first perihelion (see Chen et al. 2020), which is shown with the thick dotted line. The Athena++ simulations retain nearly constant β as they evolve (the inset zooms out to show β 0.02-GS, β 0.1-GS, and β 35-GS). Panel (b) illustrates the evolution of the normalized fluctuation amplitude, $\langle B_\perp^2 \rangle / \langle B_x \rangle^2$ (solid lines) and $\langle \rho u_\perp^2 \rangle / \langle B_x \rangle^2$ (dashed lines). The dotted–dashed line (almost directly behind the solid line for SW-Gaus) shows the WKB expectation for waves without dissipation: $B_\perp/B_x = u_\perp/v_A \propto a^{1/2}$. The dotted lines, which are read with the right-hand axis, show the normalized cross-helicity $\sigma_c = \langle \sqrt{\rho} \mathbf{u} \cdot \mathbf{B} \rangle / (\rho u^2 + B^2)$.

$|\mathbf{B}|$, resembling that at later times in the Snoopy runs. The temperature evolution in these runs is adiabatic ($c_s^2(t) \propto a^{-4/3}$), so β remains nearly constant (Figure 1(a)). We choose $\Gamma_{\text{sim}} = 0.5$ for most simulations so that wave

growth is mostly in the WKB regime, although it proved necessary to use an elongated box ($L_x = 4$, $\dot{a} = 0.5$; $\Gamma_{\text{sim}} = 2$) in the Snoopy simulations because of the enhanced dissipation over longer simulation times. We also explore a slower expansion rate $\Gamma_{\text{sim}} = 0.2$ (β 1- \dot{a} 0.2) and the same initial conditions with no expansion at all (β 1- \dot{a} 0).

3. Results

The evolved state from a selection of runs is shown in Figure 2, with a focus on β 1-Gaus-HR. The field-line visualization shows a strong switchback with a complex, three-dimensional structure, as well as sharp, angular bends along other field lines. In the spacecraft-like trace shown below (panel (c)), we see that the switchback (around $t = 0$) results in a full reversal of the magnetic field to the antisunward direction $\hat{b}_x = B_x/|\mathbf{B}| \approx +1$. The spacecraft remains in the $B_x > 0$ region for approximately 1000 s. The jumps at the boundaries of the switchback, with a scale of ~ 100 s, are resolved by only 8–10 grid cells. Because of dissipation, this ~ 100 s scale is likely around the simulation’s minimum resolvable scale. Figure 2(c) also shows that $|\mathbf{B}|$ remains fairly constant despite large changes to \mathbf{B} , as ubiquitously observed in solar-wind data (Belcher & Davis 1971; Barnes 1981; Bruno & Carbone 2013).⁴ Time traces in the lower panels illustrate several other relevant simulations. SW-Gaus resembles β 1-Gaus-HR, but with larger timescales and smoother variations due to the numerical method and lower resolution. In contrast, at high- β (β 35-GS), the tendency to maintain constant $|\mathbf{B}|$ is almost eliminated, although there remains significant variation in B_x . With no expansion (β 1- \dot{a} 0) the lack of growth of $\delta B_\perp/B_0$ means there are only small fluctuations in B_x and no reversals, while $|\mathbf{B}|$ is nearly perfectly constant.

More quantitative measures from all simulations are illustrated in Figure 3. We measure the “switchback fraction” with two methods. First, we simply count the fraction of cells with $\hat{b}_x > 0$, denoting this as $f_{\hat{b}_x > 0}$. Second, to quantify the prevalence of small-scale sharp changes in field direction, we

⁴ The small-scale oscillations at $t \approx 35,000$ s in Figure 2(c) result from a numerical instability caused by the anisotropic grid. They appear only for $a \gtrsim 3.5$ and are the reason we limit our Athena++ simulations to $a \leq 4$.

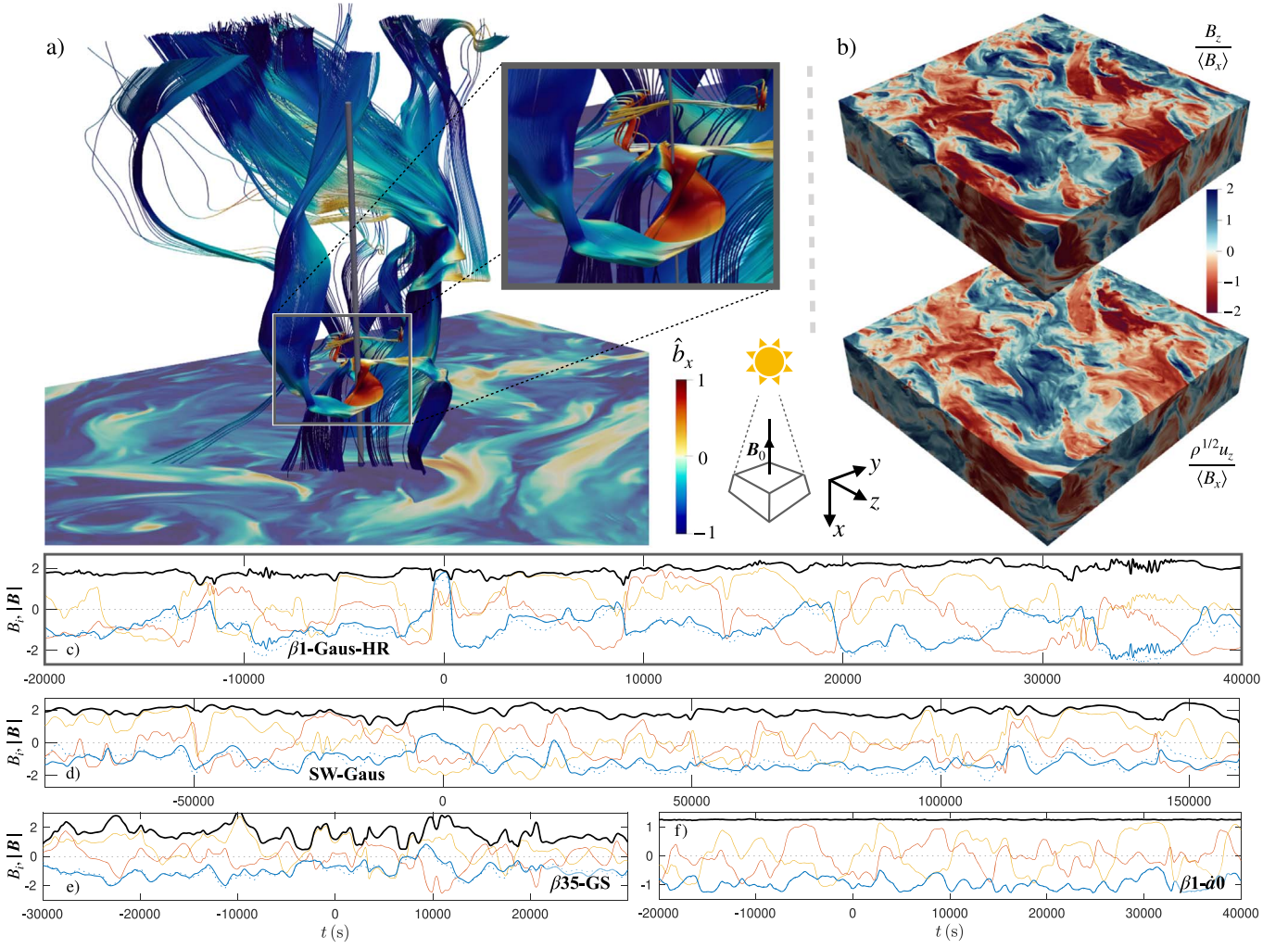


Figure 2. The magnetic-field structure in final snapshots, concentrating on $\beta 1$ -Gaus-HR (panels (a)–(c)). Panel (a) illustrates the field-line structure of a strong switchback that appears in the simulation, with the color indicating \hat{b}_x . This switchback appears to be a tangential-like discontinuity with clear 3D structure to the field lines, while a number of rotational discontinuities are visible in other regions as sharp bends in the field lines. Right-hand panels illustrate the perpendicular turbulence structure (normalized B_z and u_z), showing its sharp discontinuities and Alfvénic correlation. Panels (c)–(f) show simulated “flybys” through various simulations, scaled to solar-wind timescales using Equations (5) and (6). The flybys sample the direction $(1, 1/\sqrt{32}, -1/2\pi)$ (gray line in panel (a)) to approximate slow azimuthal motion through a fast radial-wind outflow. Black lines show $|\mathbf{B}|$, and blue, yellow, and red show B_x , B_y , and B_z , respectively, each normalized to $\langle B_x \rangle$. The dotted blue line shows $\langle B_x \rangle + u_x(4\pi\rho)^{1/2}$ (normalized by $\langle B_x \rangle$), illustrating the radial jets associated with switchbacks (Kasper et al. 2019).

calculate the probability density function of \hat{b}_x increments, $|\delta_\ell \hat{b}_x| \equiv |\hat{b}_x(\mathbf{x} + \ell) - \hat{b}_x(\mathbf{x})|$ across scale $\ell = |\ell| = L_\perp/68$ (~ 8 grid cells), and define $P(|\delta_\ell \hat{b}_x| > 1)$ as the proportion of increments with $|\delta_\ell \hat{b}_x| > 1$. Two other useful statistics are the “magnetic compression,”

$$C_{B^2} \equiv \frac{\delta \langle |\mathbf{B}|^2 \rangle}{\langle \delta \mathbf{B} \rangle^2} = \frac{\langle (|\mathbf{B}|^2 - \langle |\mathbf{B}|^2 \rangle)^2 \rangle^{1/2}}{\langle |\mathbf{B} - \langle \mathbf{B} \rangle|^2 \rangle}, \quad (7)$$

which measures the degree of spherical polarization ($|\mathbf{B}| = \text{constant}$),⁵ and the normalized fluctuation amplitude, which we define as $\langle B_\perp^2 \rangle / \langle B_x \rangle^2 = \langle B_y^2 + B_z^2 \rangle / \langle B_x \rangle^2$. We choose $\langle B_x \rangle$ to normalize the fluctuation amplitudes, as opposed to $\langle B_x^2 \rangle$ or $\langle |\mathbf{B}| \rangle$, because $\langle B_x \rangle \propto a^{-2}$ is predetermined by the expansion

⁵ Unlike the commonly used statistic $C_B \equiv \langle \delta |\mathbf{B}| \rangle / \langle \delta \mathbf{B} \rangle$ (Chen et al. 2020), C_{B^2} does not decrease with $\delta B_\perp / B_0$ for fluctuations $\delta \mathbf{B}$ oriented perpendicular to \mathbf{B}_0 . Thus, at small $\delta B_\perp / B_0$, C_{B^2} still measures correlations between field components, whereas C_B becomes a measure of the magnetosonic-mode fraction.

and $\langle B_\perp^2 \rangle / \langle B_x \rangle^2$ is not bounded from above (Matteini et al. 2018).

Figure 3(a) plots C_{B^2} and $f_{\hat{b}_x > 0}$ for all simulations and shows only modest changes to C_{B^2} as the fluctuations evolve. Comparing our primary set of $\beta \approx 1$ runs with $\beta 0.02$, $\beta 0.1$, and $\beta 35$, we see—surprisingly—that C_{B^2} is minimized around $\beta \sim 1$. We also observe that C_{B^2} increases with expansion rate (explaining the larger C_{B^2} in Snoopy runs), probably due to non-WKB growth forcing $B_\perp > u_\perp$ at large Γ_{sim} , and that C_{B^2} increases as the initial spectrum becomes steeper.

Figure 3(b) plots normalized fluctuation amplitude and $P(|\delta_\ell \hat{b}_x| > 1)$, illustrating that the increasing $\langle B_\perp^2 \rangle$ caused by expansion causes the field to become more discontinuous. The good correlation with $f_{\hat{b}_x > 0}$ (inset) shows that similar processes lead to radial-field reversals. Comparing $P(|\delta_\ell \hat{b}_x| > 1)$ between cases $\beta 35$ -GS and $\beta 1$ -GS, which have identical initial wave spectra but very different C_{B^2} , tentatively supports the hypothesis that magnetic-pressure forces, in striving to keep $|\mathbf{B}|$ constant (Vasquez & Hollweg 1998; Roberts 2012), lead to

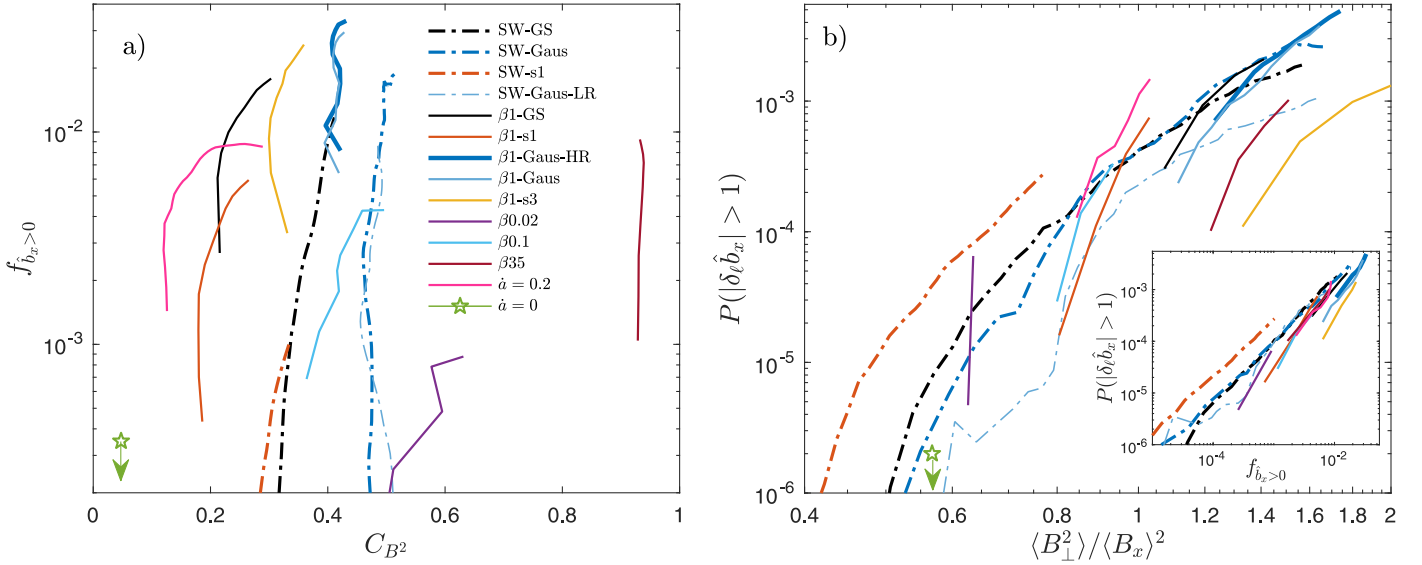


Figure 3. Key statistics from all simulations; each line shows the path of a given simulation as labeled (lines plot at $a \gtrsim 1.7$ in the Athena++ simulations to avoid the initial transient). Panel (a) compares the magnetic compressibility C_{B^2} to $f_{\hat{b}_x > 0}$, illustrating how C_{B^2} is minimized for $\beta \sim 1$ and when the expansion rate is slower. Panel (b) shows how abrupt changes in field direction, as measured by $P(|\delta_l \hat{b}_x| > 1)$, become more common as $\delta B_\perp / B_0$ grows. The inset shows the good correlation between the two switchback-fraction measures, $f_{\hat{b}_x > 0}$ and $P(|\delta_l \hat{b}_x| > 1)$. Simulation $\beta 1-\dot{a}0$ has $f_{\hat{b}_x > 0} = P(|\delta_l \hat{b}_x| > 1) = 0$ (indicated with a downward arrow).

a discontinuous field with switchbacks.⁶ We also see that: (i) at low β or with shallower initial spectra, the solutions are similarly discontinuous but the lower $f_{\hat{b}_x > 0}$ and $P(|\delta_l \hat{b}_x| > 1)$ is caused by these simulations not reaching such large amplitudes due to increased numerical dissipation (see also Figure 1(b)); (ii) lower-resolution simulations have a lower switchback fraction, especially in the Snoopy set (SW-Gaus-LR); and (iii) slower expansion ($\beta 1-\dot{a}0.2$) causes larger $f_{\hat{b}_x > 0}$ and $P(|\delta_l \hat{b}_x| > 1)$ for similar amplitudes.

Magnetic-field and velocity spectra are shown in Figure 4. Figure 4(a), which pictures SW-Gaus, shows how the spectrum flattens to around $E(k_\perp) \sim k_\perp^{-1.5}$. This is expected and in line with previous results because non-WKB growth from expansion acts like a reflection term for large-scale waves, aiding in the development of turbulence (Grappin & Velli 1996). Figure 4(b) shows the evolution of the spectral slope from a number of simulations, illustrating the general trend toward slopes around $\sim k_\perp^{-1.5}$. Although there remain some differences depending on initial conditions, and a larger difference between kinetic and magnetic spectra than seen in the solar wind (Chen et al. 2020), the spectra in runs with nonzero \dot{a} are quite similar to solar-wind spectra, despite the limited resolution of the simulations. In contrast, simulation $\beta 1-\dot{a}0$ exhibits continual steepening of the spectrum due to grid dissipation and shows no tendency to develop solar-wind-like turbulence (this is also true with $\dot{a} = 0$ and large-amplitude $\langle B_{\perp 0}^2 \rangle / B_{x0}^2 = 4$ initial conditions, which have $f_{\hat{b}_x > 0} \neq 0$; not shown). Finally, we note that the turbulence exhibits scale-dependent anisotropy similar to standard Alfvénic turbulence (Goldreich & Sridhar 1995; not shown).

Figure 5 illustrates the shape of the most intense structures in $\beta 1$ -Gaus-HR (other cases are similar). We compute $\mathbf{n}_\perp = \hat{\mathbf{x}} \times \hat{\mathbf{b}}$ and $\mathbf{n}_2 = \hat{\mathbf{n}}_1 \times \hat{\mathbf{b}}$, and use these to calculate the PDF of structures' length scales along field lines ($|\hat{\mathbf{b}} \cdot \nabla \hat{\mathbf{b}}|^{-1}$) and in the perpendicular directions ($|\hat{\mathbf{n}}_1 \cdot \nabla \hat{\mathbf{b}}|^{-1}$ and $|\hat{\mathbf{n}}_2 \cdot \nabla \hat{\mathbf{b}}|^{-1}$). A

rotational discontinuity is characterized by the scale of variation along $\hat{\mathbf{b}}$ being comparable to variation in the other directions, while a tangential discontinuity varies more rapidly in the directions perpendicular to $\hat{\mathbf{b}}$ (Neugebauer 1984). By filtering to include only regions of very large gradient as measured by the Frobenius norm ($|\nabla \hat{\mathbf{b}}|^{-1} \leq |\nabla \hat{\mathbf{b}}|_{\text{cut}}^{-1} = 4L_\perp / N_\perp$; solid lines), we see that many of the most intense structures do not exhibit sharp changes along $\hat{\mathbf{b}}$, as evidenced by the lack of a sharp peak in the PDF of $|\hat{\mathbf{b}} \cdot \nabla \hat{\mathbf{b}}|^{-1}$ at $|\nabla \hat{\mathbf{b}}|_{\text{cut}}^{-1}$ (unlike the PDFs of $|\hat{\mathbf{n}} \cdot \nabla \hat{\mathbf{b}}|^{-1}$). This shows that the most intense structures are generally tangential discontinuities, consistent with the simulated flyby and switchback illustrated in Figure 2(a).

4. Discussion

The key question that arises from our study is whether expansion and spherical polarization generically cause Alfvén waves propagating outward from the Sun to develop abrupt radial-magnetic-field reversals by the time they reach $r = 35R_\odot$, even if the initial wave field is smooth. The answer to this question is crucial for assessing what can be inferred about chromospheric and coronal processes from *PSP* measurements. Although we cannot rule out switchback formation in the low solar atmosphere, the simplicity of the in situ formation hypothesis is compelling, so long as it is consistent with observations. Our calculations clearly reproduce important basic features, including sudden Alfvénic radial-field reversals and jets, constant- $|\mathbf{B}|$ fields, and spectra around $E(k) \sim k^{-1.5}$. On the other hand, our simulations do not quite reach $f_{\hat{b}_x > 0} \approx 6\%$, as observed in *PSP* encounter 1 (Bale et al. 2019). This discrepancy, however, may simply result from lack of expansion or scale separation: $f_{\hat{b}_x > 0}$ depends on resolution (Figure 3), particularly for the Snoopy runs, which were designed to approximate the evolution of a solar-wind plasma parcel. Similarly, simulation $\beta 1-\dot{a}0.2$, which probes smaller scales,⁷

⁶ $\beta 1$ -s3, which also has lower $P(|\delta_l \hat{b}_x| > 1)$, has a somewhat steeper spectrum with less overall power at small scales; see Figure 4.

⁷ The larger dissipation in $\beta 1-\dot{a}0.2$, due to longer integration time, causes $f_{\hat{b}_x > 0}$ to be lower than the similar $\beta 1$ -GS simulation.

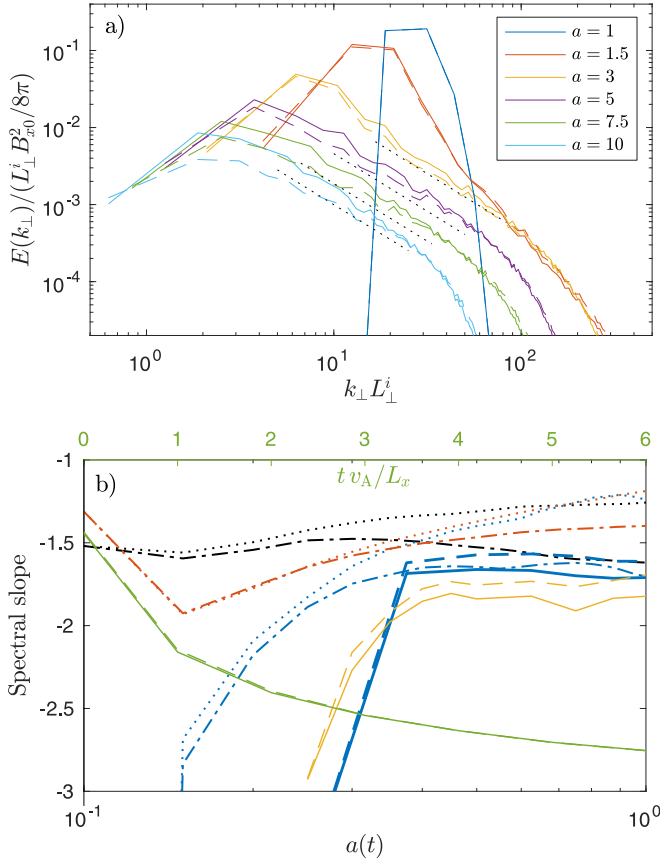


Figure 4. Broadband turbulence develops as $\delta B_{\perp}/B_0$ increases. Panel (a) shows the magnetic (solid lines) and kinetic (dashed lines) perpendicular energy spectra at six different times in SW-Gaus. The initially steep (isotropic, Gaussian) spectrum develops a clear power law $\sim k_{\perp}^{-1.5}$ (dotted black lines). Panel (b) compares the evolution of the spectral slope measured between $k_{\perp} = 50/a(t)$ and $k_{\perp} = 250/a(t)$ for various simulations (line styles as in Figure 3). There is a clear evolution toward spectra around $k_{\perp}^{-1.5}$, with shallower velocity spectra (dotted lines and dashed lines for Snoopy and Athena++ cases, respectively). The green curve with the top time axis shows $\beta_1\text{-}\hat{a}0$, which—although it exhibits very low magnetic compressibility—does not evolve toward solar-wind spectra, and does not develop an excess of magnetic energy.

exhibits larger $f_{\hat{b}_x > 0}$ and $P(|\delta \ell \hat{b}_x| > 1)$ for similar $\delta B_{\perp}/B_0$. More detailed comparison to *PSP* fluctuation statistics will be left to future work (Chhiber et al. 2020; Dudok de Wit et al. 2020; Horbury et al. 2020).

The range of magnetic compressibility C_{B^2} in our simulations broadly matches *PSP* observations on the relevant scales. A more intriguing prediction is the dependence of C_{B^2} on β (Figure 3(a)), which may be a fundamental property of MHD turbulence. While the tendency for magnetic pressure to reduce $\delta|\mathbf{B}|$ has been studied in a variety of previous works (e.g., Cohen & Kulsrud 1974; Barnes 1981; Vasquez & Hollweg 1996, 1998; Matteini et al. 2015), we believe that our observation that this tendency is strongest at $\beta \sim 1$ is new. The increase in C_{B^2} at high β is unsurprising: thermal pressure forces dominate and interfere with the magnetic-pressure driven motions that would act to reduce $\delta|\mathbf{B}|$ (absent extra kinetic effects; Squire et al. 2019). At low β , however, the larger C_{B^2} is more puzzling; we speculate on two possible reasons. First, the theory of Cohen & Kulsrud (1974) for Alfvénic discontinuities predicts a nonlinear time that approaches zero at $\beta \sim 1$ because magnetic pressure resonantly

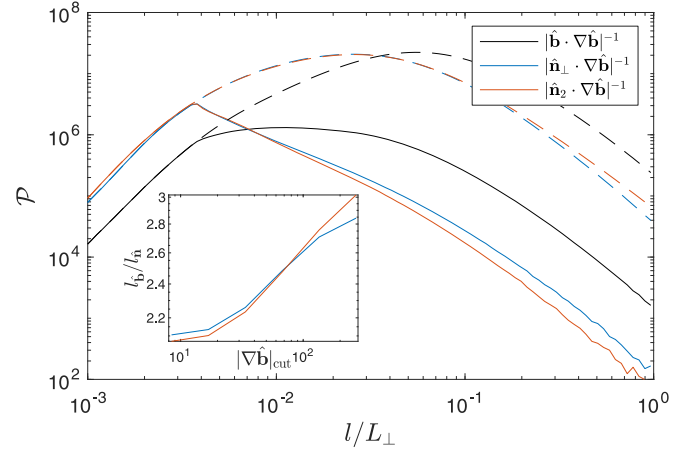


Figure 5. The statistical shapes of the most intense, switchback-like structures seen in the highest-resolution simulation β_1 -Gaus-HR. The main figure shows the PDF of the three length scales associated with each structure: field-line parallel, $l_b = |\hat{\mathbf{b}} \cdot \nabla \hat{\mathbf{b}}|^{-1}$, perpendicular in the y - z plane, $l_{\hat{n}_1} = |\hat{\mathbf{n}}_1 \cdot \nabla \hat{\mathbf{b}}|^{-1}$, and the mutually perpendicular direction, $l_{\hat{n}_2} = |\hat{\mathbf{n}}_2 \cdot \nabla \hat{\mathbf{b}}|^{-1}$. Solid lines show sharp structures, those with $|\nabla \hat{\mathbf{b}}|^{-1} \leq |\nabla \hat{\mathbf{b}}|_{\text{cut}}^{-1} = 4L_{\perp}/N_{\perp} \approx 0.1L_{\perp}$, while dashed lines show all structures with $|\nabla \hat{\mathbf{b}}|^{-1} \leq 32 \times 4L_{\perp}/N_{\perp} \approx 0.1L_{\perp}$. The PDF of $|\hat{\mathbf{b}} \cdot \nabla \hat{\mathbf{b}}|^{-1}$ does not decrease so fast with sharpness as $|\nabla \hat{\mathbf{b}}|^{-1}$, showing that the most intense structures are also more elongated in $\hat{\mathbf{b}}$, viz., they are tangential, as opposed to rotational, discontinuities. The inset shows $l_b/l_{\hat{n}_1} = \langle |\hat{\mathbf{n}}_1 \cdot \nabla \hat{\mathbf{b}}| / |\hat{\mathbf{b}} \cdot \nabla \hat{\mathbf{b}}| \rangle$ (blue line) and $l_b/l_{\hat{n}_2} = \langle |\hat{\mathbf{n}}_2 \cdot \nabla \hat{\mathbf{b}}| / |\hat{\mathbf{b}} \cdot \nabla \hat{\mathbf{b}}| \rangle$ (red line) as a function of the structure’s intensity, again measured by including only those structures with $|\nabla \hat{\mathbf{b}}| > |\nabla \hat{\mathbf{b}}|_{\text{cut}}$.

drives parallel compressions that reduce $\delta|\mathbf{B}|$. It is, however, unclear how this mechanism operates in a spectrum of oblique waves. Second, predicted parametric-decay growth rates increase at low β (Sagdeev & Galeev 1969; Goldstein 1978; Malara et al. 2000; Del Zanna 2001), which may disrupt the constant- $|\mathbf{B}|$ state and increase C_{B^2} (although this remains unclear; see Cohen & Dewar 1974; Primavera et al. 2019). Parametric-decay processes may also aid in the development of turbulence (Shoda et al. 2019). This physics, along with the role of magnetic pressure in producing discontinuous fields and switchbacks, will be investigated in future work.

5. Conclusion

We show, using expanding-box compressible MHD simulations, that a spectrum of low-amplitude Alfvén waves propagating outward from the Sun naturally develops into turbulence with many similarities to that observed in the recent perihelion passes of *Parker Solar Probe*. Some features that are reproduced by our simulations include the presence of abrupt radial-magnetic-field reversals (switchbacks) associated with jumps in radial velocity, nearly constant magnetic-field strength, and energy spectra with slopes around $k_{\perp}^{-1.5}$. We present two sets of simulations with complementary numerical methods: the first (SW-# in Table 1) follows a parcel of plasma through a factor-of-10 expansion, with waves growing from linear to nonlinear amplitudes; the second (β #-#) explores the dependence of expansion-driven turbulence on initial conditions, β , and expansion rate.

Our key results can be summarized as follows:

- (i) Switchbacks can form “in situ” in the expanding solar wind from low-amplitude outward-propagating Alfvénic fluctuations that grow in normalized amplitude due to radial expansion. This indicates that *PSP* observations are

broadly consistent with a natural state of large-amplitude imbalanced Alfvénic turbulence. The strongest switchbacks are tangential-like discontinuities.

- (ii) The magnetic field develops correlations between its components in order to maintain constant $|\mathbf{B}|$ (Vasquez & Hollweg 1998). We show that this effect, which has been extensively documented in observations, is strongest at $\beta \sim 1$, absent at high β , and reduced for $\beta \ll 1$.
- (iii) Imbalanced Alfvénic turbulence, with energy spectra $\sim k_{\perp}^{-1.5}$ and scale-dependent anisotropy, develops from homogeneous, random, outward-propagating Alfvén waves in the compressible expanding-box model.

We hypothesize that (i) results from (ii)—i.e., that switchbacks result from the combination of spherical polarization and expansion-induced growth in $\delta B_{\perp}/B_0$ —because discontinuities are a natural result of large- $\delta B_{\perp}/B_0$ fluctuations with constant $|\mathbf{B}|$ (Roberts 2012; Valentini et al. 2019).

To more thoroughly assess the in-situ switchback-formation hypothesis and compare detailed statistical measures with observations, two important numerical goals for future work are to run to larger expansion factors without excessively fast expansion or high dissipation, and to reach the steady state where turbulent dissipation balances expansion-driven wave growth. This will require long simulation times at high resolution. Including mean-azimuthal-field growth (the Parker spiral) and/or improved expansion models (e.g., Tenerani & Velli 2017) may also be necessary. Theoretically, significant questions remain regarding the mechanisms for reducing $\delta|\mathbf{B}|$ (Cohen & Kulsrud 1974; Vasquez & Hollweg 1998).

We thank Stuart Bale, Chris Chen, Tim Horbury, Justin Kasper, Benoit Lavraud, Lorenzo Matteini, Anna Tenerani, and Marco Velli for helpful discussions. Support for J.S. and R.M. was provided by Rutherford Discovery Fellowship RDF-U001804 and Marsden Fund grant UO01727, which are managed through the Royal Society Te Apārangi. B.C. was supported in part by NASA grants NNX17AI18G and 80NSSC19K0829 and NASA grant NNN06AA01C to the *Parker Solar Probe* FIELDS Experiment. High-performance computing resources were provided by the New Zealand eScience Infrastructure (NeSI) under project grant uo02637 and the PICSciE-OIT TIGRESS High Performance Computing Center and Visualization Laboratory at Princeton University. This work was started at the Kavli Institute for Theoretical Physics in Santa Barbara, which is supported by the National Science Foundation under grant No. NSF PHY-1748958.

ORCID iDs

J. Squire  <https://orcid.org/0000-0001-8479-962X>
 B. D. G. Chandran  <https://orcid.org/0000-0003-4177-3328>
 R. Meyrand  <https://orcid.org/0000-0002-8327-5848>

References

- Bale, S. D., Badman, S. T., Bonnell, J. W., et al. 2019, *Natur*, 576, 237
 Barnes, A. 1981, *JGR*, 86, 7498
 Belcher, J. W., & Leverett, D. 1971, *JGR*, 76, 3534
 Bruno, R., & Carbone, V. 2013, *LRSF*, 10, 2
 Chandran, B. D. G., Dennis, T. J., Quataert, E., & Bale, S. D. 2011, *ApJ*, 743, 197
 Chandran, B. D. G., & Perez, J. C. 2019, *JPIPh*, 85, 905850409
 Chen, C. H. K., Bale, S. D., Bonnell, J. W., et al. 2020, *ApJS*, 246, 53
 Chhiber, R., Goldstein, M. L., Maruca, B. A., et al. 2020, *ApJS*, 246, 31
 Cho, J., Lazarian, A., & Vishniac, E. T. 2002, *ApJ*, 564, 291
 Cohen, R. H., & Dewar, R. L. 1974, *JGR*, 79, 4174
 Cohen, R. H., & Kulsrud, R. M. 1974, *PhFI*, 17, 2215
 Del Zanna, L. 2001, *GeoRL*, 28, 2585
 Dong, Y., Verdini, A., & Grappin, R. 2014, *ApJ*, 793, 118
 Dudok de Wit, T., Krasnoselskikh, V. V., Bale, S. D., et al. 2020, *ApJS*, 246, 39
 Goldreich, P., & Sridhar, S. 1995, *ApJ*, 438, 763
 Goldstein, M. L. 1978, *ApJ*, 219, 700
 Grappin, R., & Velli, M. 1996, *JGR*, 101, 425
 Grappin, R., Velli, M., & Mangeney, A. 1993, *PhRvL*, 70, 2190
 Horbury, T. S., Matteini, L., & Stansby, D. 2018, *MNRAS*, 478, 1980
 Horbury, T. S., Woolley, T., Laker, R., et al. 2020, *ApJS*, 246, 45
 Kasper, J. C., Bale, S. D., Belcher, J. W., et al. 2019, *Natur*, 576, 228
 Lesur, G., & Longaretti, P. Y. 2007, *MNRAS*, 378, 1471
 Malara, F., Primavera, L., & Veltri, P. 2000, *PhPI*, 7, 2866
 Maron, J., & Goldreich, P. 2001, *ApJ*, 554, 1175
 Matteini, L., Horbury, T. S., Pantellini, F., Velli, M., & Schwartz, S. J. 2015, *ApJ*, 802, 11
 Matteini, L., Stansby, D., Horbury, T. S., & Chen, C. H. K. 2018, *ApJL*, 869, L32
 Mignone, A. 2007, *JCoPh*, 225, 1427
 Montagud-Camps, V., Grappin, R., & Verdini, A. 2018, *ApJ*, 853, 153
 Neugebauer, M., Clay, D. R., Goldstein, B. E., Tsurutani, B. T., & Zwickl, R. D. 1984, *JGR*, 89, 5395
 Neugebauer, M., & Goldstein, B. E. 2013, in AIP Conf. Ser. 1539, Solar Wind 13, ed. G. P. Zank et al. (Melville, NY: AIP), 46
 Perez, J. C., & Chandran, B. D. G. 2013, *ApJ*, 776, 124
 Primavera, L., Malara, F., Servidio, S., Nigro, G., & Veltri, P. 2019, *ApJ*, 880, 156
 Roberts, D. A. 2012, *PhRvL*, 109, 231102
 Roberts, M. A., Uritsky, V. M., DeVore, C. R., & Karpen, J. T. 2018, *ApJ*, 866, 14
 Sagdeev, R. Z., & Galeev, A. A. 1969, *Nonlinear Plasma Theory* (New York: Benjamin)
 Shi, C., Velli, M., Tenerani, A., Rappazzo, F., & Réville, V. 2020, *ApJ*, 888, 68
 Shoda, M., Suzuki, T. K., Asgari-Targhi, M., & Yokoyama, T. 2019, *ApJL*, 880, L2
 Squire, J., Schekochihin, A. A., Quataert, E., & Kunz, M. W. 2019, *JPIPh*, 85, 905850114
 Stone, J. M., Gardiner, T. A., Teuben, P., Hawley, J. F., & Simon, J. B. 2008, *ApJS*, 178, 137
 Tenerani, A., & Velli, M. 2017, *ApJ*, 843, 26
 Tenerani, A., Velli, M., Matteini, L., et al. 2020, *ApJS*, 246, 32
 Valentini, F., Malara, F., Sorriso-Valvo, L., Bruno, R., & Primavera, L. 2019, *ApJL*, 881, L5
 van Ballegoijen, A. A., Asgari-Targhi, M., Cranmer, S. R., & DeLuca, E. E. 2011, *ApJ*, 736, 3
 Vasquez, B. J., & Hollweg, J. V. 1996, *JGR*, 101, 13527
 Vasquez, B. J., & Hollweg, J. V. 1998, *JGRA*, 103, 335
 White, C. J., Stone, J. M., & Gammie, C. F. 2016, *ApJS*, 225, 22